Tracking of Migrating Cells Under Phase-Contrast Video Microscopy With Combined Mean-Shift Processes

O. Debeir*, P. Van Ham, R. Kiss, and C. Decaestecker

***Abstract*—In this paper, we propose a combination of mean-shift-based tracking processes to establish migrating cell trajectories through *in vitro* phase-contrast video microscopy. After a recapitulation on how the mean-shift algorithm permits efficient object tracking we describe the proposed extension and apply it to the *in vitro* cell tracking problem. In this application, the cells are unmarked (i.e., no fluorescent probe is used) and are observed under classical phase-contrast microscopy. By introducing an adaptive combination of several kernels, we address several problems such as variations in size and shape of the tracked objects (e.g., those occurring in the case of cell membrane extensions), the presence of incomplete (or noncontrasted) object boundaries, partially overlapping objects and object splitting (in the case of cell divisions or mitoses). Comparing the tracking results automatically obtained to those generated manually by a human expert, we tested the stability of the different algorithm parameters and their effects on the tracking results. We also show how the method is resistant to a decrease in image resolution and accidental defocusing (which may occur during long experiments, e.g., dozens of hours). Finally, we applied our methodology on cancer cell tracking and showed that cytochalasin-D significantly inhibits cell motility.**

***Index Terms*—Cell division, cell motility, image processing, mean-shift, tracking, video microscopy.**

I. Introduction

A. Automatic Cell Motility Analysis

IN VITRO cell displacement has been shown to be a useful parameter to consider in several biological applications, such as the study of cell migration and its variations under different culture conditions or drug actions (e.g., see [1]–[5]). To analyze cell migration, it is usual to automatically record sequences of frames by means of microscopes equipped with video acquisition systems. The locations of each cell have to be tracked during entire sequences and qualitative and quantitative features have to be computed (average speed, maximum displacement, etc.). Manual or interactive computer-assisted tracking has been used by many authors [6]–[9]. However, this approach quickly becomes a tedious task if a large number of cells must be tracked during long periods (dozens of hours) in order to obtain statistically robust results. This is why automation is becoming increasingly popular [5], [10]–[15]. Unfortunately, some acquisition modalities, imposed by the tackled biological problem, give poor image quality for automatic image processing (e.g., phase-contrast imaging in our case), leading to nonobvious image analysis problems that remain an interesting issue. Furthermore, tracking algorithms able to work on gray-level images acquired from standard cell cultures exempt the users from having recourse to fluorescent markers, as used by certain authors (e.g., [10]).

A number of works aiming to quantify cell motility use a monolayer wound model (see, e.g., [1] and [16]). This consists in wounding a confluent monolayer of cells and then evaluating cell migration (usually on the basis of timelapse image recording) either by determining the rate of advance of the wound edge as a measurement of the rate of cell locomotion [1], or by counting the number of migrating cells (i.e., the number of cells observed across the wound borders) [16]. This kind of assay does not consider individual cell locomotion nor does it distinguish between the roles played by cell migration and cell proliferation in the advance of the wound edge. While the wound approach is particularly well adapted to model cell response to a lesion occurring in a tissue, individual cell migration assay is more adapted for biological mechanisms involving individual cells (such as inflammatory and immune reactions, and tumor spreading and metastasis). These mechanisms are concerned in the present application where the aim is to follow individual living cells during dozens of hours and to construct their trajectories from a set of successive positions that we call "cell centroids." Experimental observations showed that the cell centroids chosen by human experts (i.e., cell biologists) correspond to points located near the centers of the cell soma. As illustrated in Fig. 1, on various cell cultures, the cell soma generally appears as a dark area surrounded by a white halo (under phase contrast imaging). However, this kind of pattern often appears at various places in a single cell. To help to identify a good initial centroid for each cell, the first instance of each cell position will be determined by a human operator on the first frame of the sequence and will be used as the initial conditions of the tracking process (see Section III-B). Our aim is then to identify a dark area surrounded by a white halo in

Manuscript received November 8, 2003; revised February 21, 2005. The Associate Editor responsible for coordinating the review of this paper and recommending its publication was N. Ayache. *Asterisk indicates corresponding author.*

*O. Debeir is with the Department of Logical and Numerical Systems, Faculty of Applied Sciences, CP 165/57, Université Libre de Bruxelles, 50 Av. F. Roosevelt, 1050 Brussels, Belgium (e-mail: odebeir@ulb.ac.be).

P. Van Ham is with the Department of Logical and Numerical Systems, Faculty of Applied Sciences, Université Libre de Bruxelles, 1050 Brussels, Belgium (e-mail: pavaha@ulb.ac.be).

R. Kiss and C. Decaestecker are with Laboratory of Toxicology, Institute of Pharmacy, Université Libre de Bruxelles, 1050 Brussels, Belgium (e-mail: rkiss@ulb.ac.be; cdecaes@ulb.ac.be). They are also with the Belgian National Fund for Scientific Research, FNRS, Brussels, Belgium.

Digital Object Identifier 10.1109/TMI.2005.846851

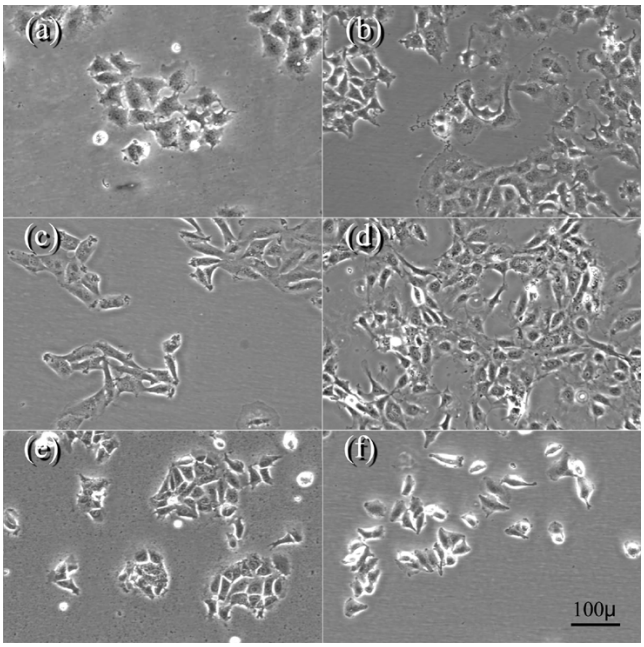

Fig. 1. Examples of observed images on different cell cultures under phase contrast imaging. Cells appear as dark areas surrounded by bright halos. These halos are sometimes difficult to see on the recorded images [e.g., see frame (a)]. The preprocessing steps used in our application clearly highlight them (see Fig. 7). The human cell lines illustrated (and their origins) are (a) MCF7 (breast carcinoma). (b) U373MG (high grade astrocytoma). (c) U87MG (high grade astrocytoma). (d) HUVEC (human umbilical vein endothelial cells). (e) HCT15 (melanoma). (f) A549 (colon carcinoma). All the cancer cell lines (i.e., all except the HUVEC primoculture) were obtained from the American Type Culture Collection (ATCC, Manassas, VA). For details about cell cultures, see [2-4].

the neighborhood of each centroid and then track the centers of this kind of pattern from frame to frame.

B. Tracking by Segmentation and Model Tracking

There are two main approaches described in literature that tackle (biological) object tracking.

The first way is frame-by-frame image segmentation tracking (e.g., see [11]–[13], and [17]). The first segmentation phase consists in automatically detecting object candidates on a given frame on the basis of their specific properties (border, texture, color. . .). After this, a between-frames object-pairing is carried out in order to follow each object displacement during the sequence of frames. This approach is efficient when object borders are sharp and is useful for temporal and spatial sequences as well (e.g., where the time axis is replaced by the z axis). As the segmentation in each frame may be independent from the other frames, it is possible to handle objects with a changing topology (in our case during mitoses, i.e., when a mother cell splits into two daughter cells) but handling contiguous and overlapping objects may become difficult. In our application, partially overlapping objects are often encountered. Furthermore, image quality (under phase-contrast microscopy) does not ensure sharp borders of the tracked objects. This is why we investigated another approach described in Section II.

The second way deals with object model adjustment. This essentially consists in optimizing a parameterized model shape in order to fit the model to the targeted objects (i.e., each cell in a frame in this case). This type of method does not find all possible objects in the frame, but focuses on one unique candidate (which corresponds to the predefined model) located around an initial position. "Active contours" (or "Snakes") [5], [10], [14], [15] is such a method, and also gives, as a secondary result, a segmentation of the objects. "Level sets", a more general approach, are able to tackle object topology changes [18] but present other drawbacks for cell tracking [5]. The mean-shift algorithms give a fast solution for object tracking in video sequences (e.g., vehicle tracking, closed loop video) [19], [20], but usually do not give object contours. Different methods can be combined such as mixing the mean-shift and active contour approaches [21]. In contrast to segmentation-based methods, this second group of methods does not require a between-frames object-pairing stage in the processing of temporal sequences. Indeed, the result of the model adjustment process in frame t-1 is used to initialize the process in frame t [5], [10], [14], [15], [19], [20]. This straightforward automatic initialization trivially links object positions across frames if the objects move relatively little between consecutive frames (this can be easily satisfied by adjusting the number of frames acquired by time unit). The object positions on the first frame of the sequence have also to be identified to initialize the complete process (e.g., easily done manually).

C. Our Approach: The Combination of Several Model-Based Mean-Shift Processes

In the context of our application, i.e., tracking migrating cells, we do not focus on object segmentation but rather on the tracking of object positions (located by what we call "centroids"). We do not emphasize the precise border detection for the following reasons. First, phase contrast microscopy produces bright halos (see Fig. 1) around the observed objects whose thickness greatly depends on the focus plane. Second, migrating cells often present membrane extensions out of the focal plane. In this case, the cell borders do not appear as a continuum. Third, cells can interact closely with each other and, thus, parts of their borders can be merged. Finally, cells which undergo division present splits of their borders to two different contours (one per daughter cell). All these facts make the tracking of cells with methods based on object border detection difficult. It results that "active contours" and "level sets" methods require a larger number of adaptations to be successfully applied (see [5] for details). This is why we consider the border location rather as a qualitative data and promote the use of an alternative approach, based on the mean-shift method, to track, from one frame to the next, the new position of each object. In Section II, we show how to combine several mean-shift processes to follow complex gray level patterns. We, therefore, build an adaptive combination of such processes based on an ensemble of nested kernels attracted by either black or white pixels, and we detail how to determine and adapt these kernels to be able to follow living cells despite their morphological changes and divisions. In Section III, we specify some particular points linked to our application (such as image acquisition and preprocessing). In Section IV we validate our algorithm by comparing results obtained by means of the automatic tracking algorithm with those generated manually by a human expert. We also used this

approach to test the algorithm robustness with respect to the different parameters used in our adaptive model. In Section V, we present a biological application of the effects of a specific drug on the motility of tumor cells. Our conclusion is drawn in Section VI.

II. Mean-Shift Algorithm

A. General Mean-Shift

Mean-shift generalized in [22] is a simple iterative procedure that fundamentally seeks to identify a local mode within a set of data. This is based on the notion of "kernel." Briefly, if $K(\mathbf{x})$ is a flat kernel of radius λ centered on $\mathbf{x}$ which is defined in the n-dimensional Euclidian space as

$$K(\mathbf{x}) = \begin{cases} 1, & \text{if } \|\mathbf{x}\| \leq \lambda \\ 0 & \text{if } \|\mathbf{x}\| > \lambda \end{cases}$$

and the sample mean at $\mathbf{x}$ for a finite data set S is

$$\mathbf{m}(\mathbf{x}) = \frac{\sum_{\mathbf{s}\in S} K(\mathbf{s}-\mathbf{x})\mathbf{s}}{\sum_{\mathbf{s}\in S} K(\mathbf{s}-\mathbf{x})}$$

The mean-shift is the difference $\mathbf{m}(\mathbf{x}) - \mathbf{x}$. The algorithm consists in iteratively replacing the current kernel position $\mathbf{x} \leftarrow \mathbf{m}(\mathbf{x})$, i.e., shifts it to the average of data points computed in its neighborhood (which is defined by the kernel).

Fig. 2 illustrates the application of a mean-shift process on a gray-level image. Fig. 2(a) shows a two-dimendsional (2-D) data set represented as a gray-level image lattice where bright pixels (high gray levels) correspond to high densities and dark to low ones. The flat kernel used is a disk whose initial position is located by the bounding black square shown in Fig. 2(a). With respect to this kernel attracted by the bright pixels, the sample mean $\mathbf{m}(\mathbf{x})$ is computed as follows:

$$\mathbf{m}(\mathbf{x}) = \frac{\sum_{\mathbf{p}} K(\mathbf{p}-\mathbf{x})g(\mathbf{p})\mathbf{p}}{\sum_{\mathbf{p}} K(\mathbf{p}-\mathbf{x})g(\mathbf{p})}$$

where $\mathbf{p}$ is any pixel of the image and $g(\mathbf{p})$ its gray level. The simple iteration process converges toward the central part of the gray-level distribution [see the black disk in Fig. 2(a)]. The same process is also applied with a kernel attracted by the dark pixels [see the white square and disk in Fig. 2(a)] after having inverted the gray-level value $g(\mathbf{p})$ of each pixel $\mathbf{p}$ (i.e., using $255 - g(\mathbf{p})$ for a 8 bit grayscale image), showing how the kernels escape from the high intensities area to a low one.

Mean-shift is, thus, a very convenient method to locally find the brightest (or the darkest) area in a gray-level image. Theoretical results have been provided concerning the convergence of the algorithm for flat and Gaussian kernels and the link with gradient ascent/descent techniques [22]. In Sections II-B to II-D, we focus on image application of the mean-shift process with the density interpretation of the gray levels. We, thus, adapt this approach in order to detect particular gray level patterns in an image.

B. Coupled Mean-Shifts

Now let us consider a mean-shift-based method which couples two (or more) kernels in order to detect gray-level configurations which are more complex than those illustrated in Fig. 2(a). At this point, the proposed algorithm is slightly different to the standard mean-shift one in the sense that the new position of a center $\mathbf{x}$ is not defined by the sample mean computed on one kernel but by the averaged position of two (or more) sample means computed on different and linked kernels. Fig. 2(b) shows the result obtained with two linked kernels K_1 and K_2, which are attracted by bright and dark pixels respectively (where inverted gray levels are used in the case of K_2, as introduced in Section II-A). The centers of both kernels (labeled $\mathbf{m}_1$ and $\mathbf{m}_2$, respectively), thus, move together according to the equations shown below (for an 8-bit grayscale image)

$$\mathbf{m}_1(\mathbf{x}) = \frac{\sum_{\mathbf{p}} K_1(\mathbf{p}-(\mathbf{x}+\mathbf{o}_1))g(\mathbf{p})\mathbf{p}}{\sum_{\mathbf{p}} K_1(\mathbf{p}-(\mathbf{x}+\mathbf{o}_1))g(\mathbf{p})}$$

$$\mathbf{m}_2(\mathbf{x}) = \frac{\sum_{\mathbf{p}} K_2(\mathbf{p}-(\mathbf{x}+\mathbf{o}_2))(255-g(\mathbf{p}))\mathbf{p}}{\sum_{\mathbf{p}} K_2(\mathbf{p}-(\mathbf{x}+\mathbf{o}_2))(255-g(\mathbf{p}))}$$

where $\mathbf{o}_i$ is the offset of each kernel to the origin of the coupled model. The iteration becomes

$$\mathbf{x} \leftarrow \mathbf{m}(\mathbf{x}) = \frac{\mathbf{m}_1(\mathbf{x}) + \mathbf{m}_2(\mathbf{x})}{2}.$$

This kernel couple is, thus, able to find borders between contrasted regions [Fig. 2(b)]. In Section II-D, we will describe how to adapt this mean-shift combination to track our objects of interest (i.e., *in vitro* cells) which often appear as black objects surrounded by white halos but may change into bright objects surrounded by a dark background.

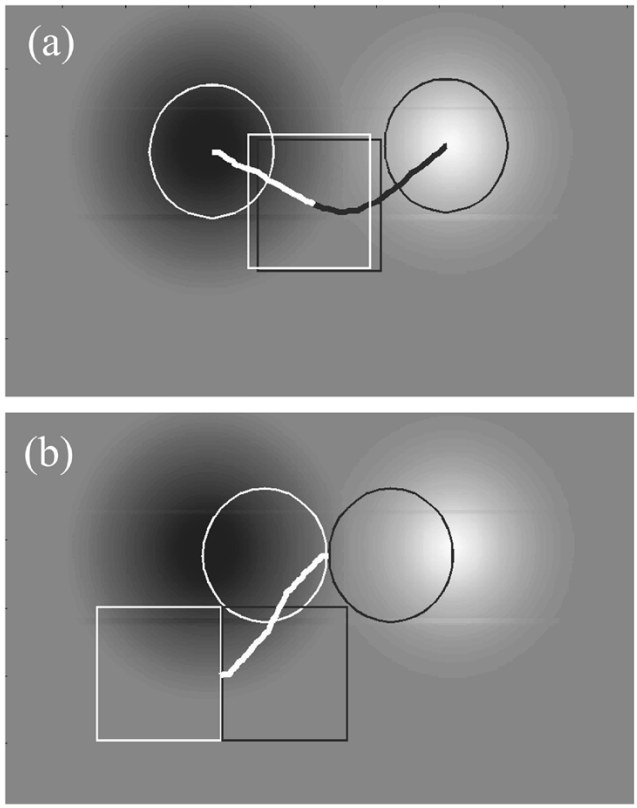

Fig. 2. Two-dimensional mean-shift examples. (a) Illustration of two independent mean-shift processes carried out on a 2-D-distribution, each using a flat disk kernel respectively attracted by white or dark pixels. The initial locations of the kernels are shown by squares (surrounding the initial disks) and the final by the disks themselves (the resulting mean-shifts are indicated by the black and white segments). Both trajectories are indicated by lines from the common initial kernel centers to the final ones. (b) Coupled mean-shifts based on linked kernels. The line shows the trajectory covered by the "mean" of the coupled kernels from the initial to the final locations (see text).

C. Adaptive Combination of Linked Kernels

Previous works proposed methods based on scale space representation [20] where the kernel size is one of the parameters of the mean-shift algorithm. This approach gives algorithms robust enough to resist changes in the size of the tracked objects. Because of application reasons detailed in Section II-E we want the tracking algorithm to remain resistant to huge changes in the appearance of the tracked objects. Typically we want to design an algorithm able to track an object as long as possible, knowing that the object generally presents a type of gray-level configuration (e.g., a black area surrounded by a white halo) which may change to another type (e.g., a small bright area surrounded by a dark background) during a certain time interval. We propose to use different combinations of mean-shift algorithms, like the one described in Section II-B. Each combination is based on a set of kernels K_i and their respective weights w_i in the combined model. The shift is defined by

$$\mathbf{x} \leftarrow \mathbf{m}(\mathbf{x}) = \frac{\sum_i w_i \mathbf{m}_i(\mathbf{x})}{\sum_i w_i} \tag{1}$$

where $\mathbf{m}_i(\mathbf{x})$ is the mean sample computed on K_i.

We choose to use a unique set of kernels (with adaptive sizes, see Section II-D) and introduce variations in the weights which determine their combination. A given set of weights, represented as a weight vector $\mathbf{W} = (w_1, \ldots, w_i, \ldots, w_n)^{\mathrm{T}}$, is associated with a specific gray level pattern (e.g., dark-surrounded-by-bright). To be able to track a given object presenting changes in its gray-level configuration, we propose using an adaptive combination determined as follows. For example, let us consider two different configurations (i.e., kernel combinations) characterized by two different weight vectors (labeled $\mathbf{W}$ and $\mathbf{W}'$). A mix of both weight vectors determines the adaptive combination enabling the transition from one configuration to the other

$$\mathbf{W}^* = \alpha \mathbf{W} + (1 - \alpha)\mathbf{W}' \tag{2}$$

where parameter α is a function of the current object shape or size depending on the application (see Section II-D).

D. Chosen Adaptive Kernels and Their Combination

Here, we detail the two adaptation levels introduced in our model in order to be able to track living cells under phase-contrast microscopy imaging. First, we show how to modify the sizes and shapes of the kernels used to take into account the possible variations in cell morphology. Second, we show in detail how to adapt the weight vector of the kernel combination [see (2)] to allow the transition between two different gray-level patterns encountered during cell mitosis.

Our adaptive model is in fact controlled by several parameters whose values essentially depend on general cell and image features, such as the range of cell sizes encountered in regards to the image resolution used. The different parameter values summarized in Table I were used with success on various cell types including essentially tumor cells of various origins [Fig. 1(a)–(c) and (e)–(f)] and nontumoral endothelial cells [Fig. 1(d)]. As detailed in Table I, certain parameters are scale-dependent and, thus, their values are adapted to the magnification ratio and image resolution detailed in Section III-A. The robustness of the algorithm according to these parameter values is illustrated in Section IV-B.

TABLE I
ALGORITHM AND PREPROCESSING PARAMETERS

	Parameter	Symbol	Equation	Typical value*[1]	Measurement unit
ALGORITHM	Number of kernel sectors	*ndir*		8	-
	Kernel weight vector normal cell model	**W**	(2)	(0.2, 0.8, 0)	-
	Kernel weight vector mitotic cell model	**W'**	(2)	(0.7, 0.2, 0.1)	-
	Model expansion factor	k	(3)	1.55	-
	Anisotropy level	β	(3)	0.05	-
	Sigmoid threshold	d^*	(4)	15 (13.8)*[2]	pixel (µm)*[2]
	Sigmoid slope	s	(4)	0.75 (0.69)	pixel^{-1} (µm^{-1})
Pre-Processing	Gradient radius			15 (13.8)	pixel (µm)
	Gray level threshold			50	(8-bit scale)
	Equalization radius			20 (18.4)	pixel (µm)

*[1] see sections IV.B and IV.C for robustness analysis.
*[2] for the scale-dependent parameters, the default values expressed in pixels are also translated in µm in order to be independent of the magnification ratio (in our images 1 pixel = 0.92 µm, see section III.A).

As mentioned in Section I, the tracked cells are roughly black objects surrounded by bright halos. In a first approach, we use the model described in Fig. 3(a) where two mean-shift processes based on two nested kernels are combined. The first kernel is attracted by the bright pixels (of high intensities) and is composed of ndir triangles (we use $\mathrm{ndir} = 8$), labeled A_{wi} (where index "w" means "white"), with different heights (r_{wi}) connected at the centroid of the cell (x_0, y_0). These triangles define an irregular apple-pie-like kernel labeled K_1. The second nested kernel K_2 is made up of ndir smaller triangles A_{bi} (where index "b" means "black") also centered in (x_0, y_0). In order to have a mean-shift attracted by the darkest part of the image, the gray levels are inverted $(255 - g(\mathbf{p}))$ in this second kernel. The heights of these smaller triangles, labeled r_{bi}, are equal to a fraction of the corresponding r_{wi} (we use $r_{bi} = 0.5 r_{wi}$). The "black-tracking" kernel, thus, remains nested into the "white-tracking" kernel. The iterative process uses (1), where $i = 1, 2$, to compute the new cell centroid in frame t from an initial location $\mathbf{x}_0$, which corresponds to the centroid location identified in frame $(t-1)$. The weights (w_1 and w_2) in (1) are constant (and scale-independent). Values such as $w_1 = 0.2$ and $w_2 = 0.8$ were successfully used to track various types of cells as long as the cells did not enter division (as explained later).

To take into account the possible variations in cell shape and size from frame t to the next $(t+1)$, the kernels are submitted to deformations. To these aims, the different heights r_{wi} of the A_{wi} triangles are adapted (for each cell) on the basis of the distribution of the mass centers of these triangles. Briefly, given a model centered on a cell in frame t, the mass centers $\mathbf{g}_{wi}(t)$ of each triangle $A_{wi}(t)$ are computed. These mass centers [see the black vertices in Fig. 3(a)] define a polygon centered on the cell centroid and attached to the bright halo. A nested polygon attached to the dark inner part can be similarly defined by the mass centers of the A_{bi} triangles [see the white vertices in Fig. 3(a)].

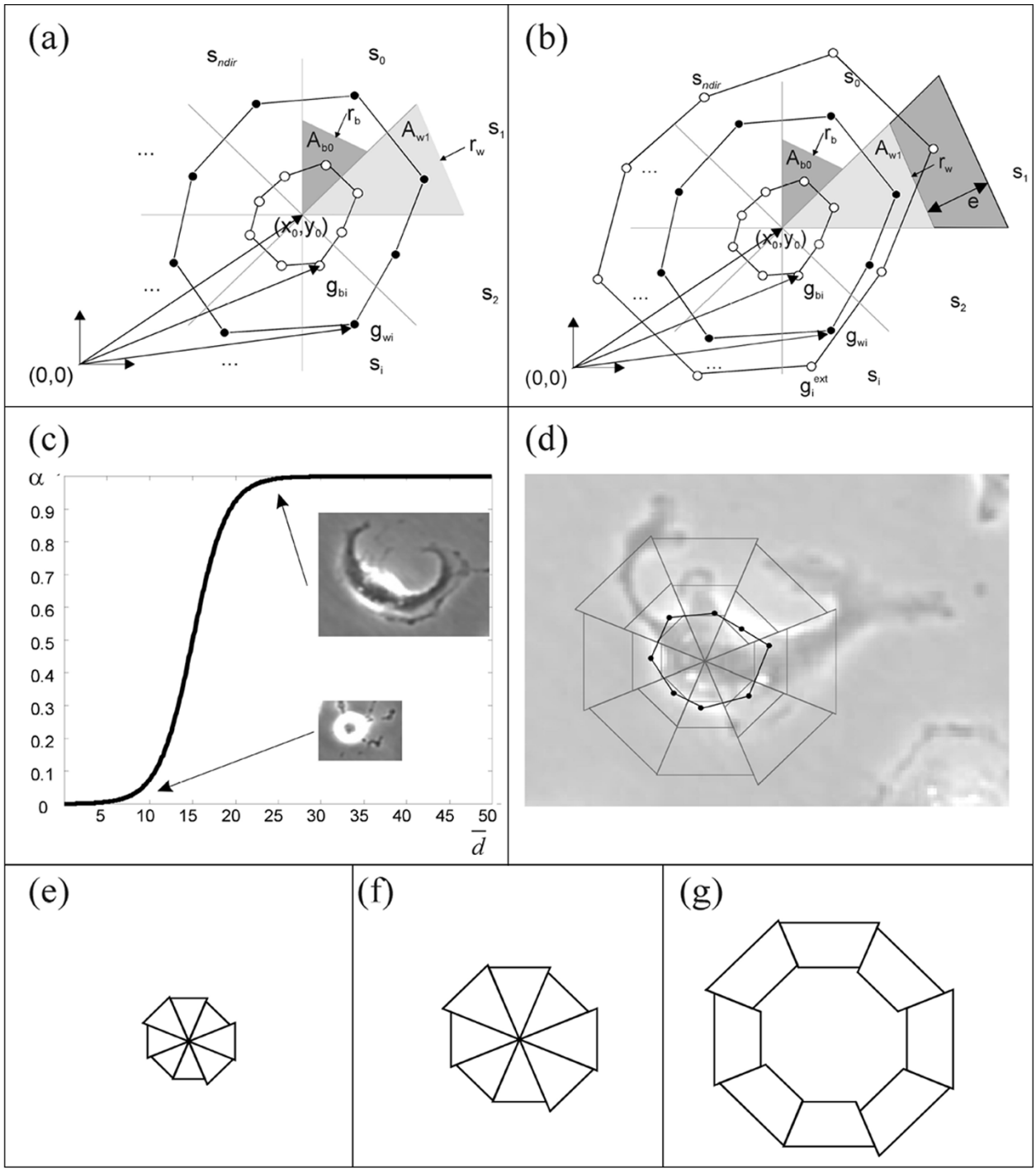

Fig. 3. Illustrations of the mean-shift models used. Models with (a) two nested kernels and (b) an additional external kernel (see text). (c) Variation of the α parameter used in (2) as a function of $\bar{d}$, which is the mean distance between the cell centroid and the $\mathbf{g}_{wi}$ mass centers [i.e., the black vertices shown in (a) and (b)]. This ensures a transition between two models attracted by two different gray-level patterns characterizing either a cell during a mitotic process (small $\bar{d}$) or in a normal migrating process (larger $\bar{d}$, see text). (d) 3-kernels model adjusted on a cell including the $\mathbf{g}_{wi}$ mass centers and the corresponding polygon, and the areas corresponding to (e) kernel K_2 (attracted by the inner dark pixels). (f) Kernel K_1 (attracted by the white pixels). (g) Kernel K_3 (attracted by the external dark pixels), respectively.

To adapt the kernel used in frame $(t+1)$, each $r_{wi}(t)$ value is updated to $r_{wi}(t+1)$

$$r_{wi}(t+1) = k(\beta\bar{d}(t) + (1-\beta)d_i(t)) \tag{3}$$

where $k > 1, \beta < 1$ (we use $k = 1.55$ and $\beta = 0.05$), and $\bar{d}(t)$ is the average of the distances $d_i(t)$ between the different $\mathbf{g}_{wi}(t)$ and the cell centroid $\mathbf{c}(t)$ determined in frame t.

This maintains a certain level of anisotropy in the kernel (in the directions established in frame t) which avoids too large coverings between the kernels centered on the different cells. This is particularly useful when the cells have a lengthened morphology and are very close (see Section II-E). Factor k must be larger than 1 in order to track objects increasing in size. The corresponding radii $r_{bi}(t+1)$ of the nested A_{bi} triangles are adapted

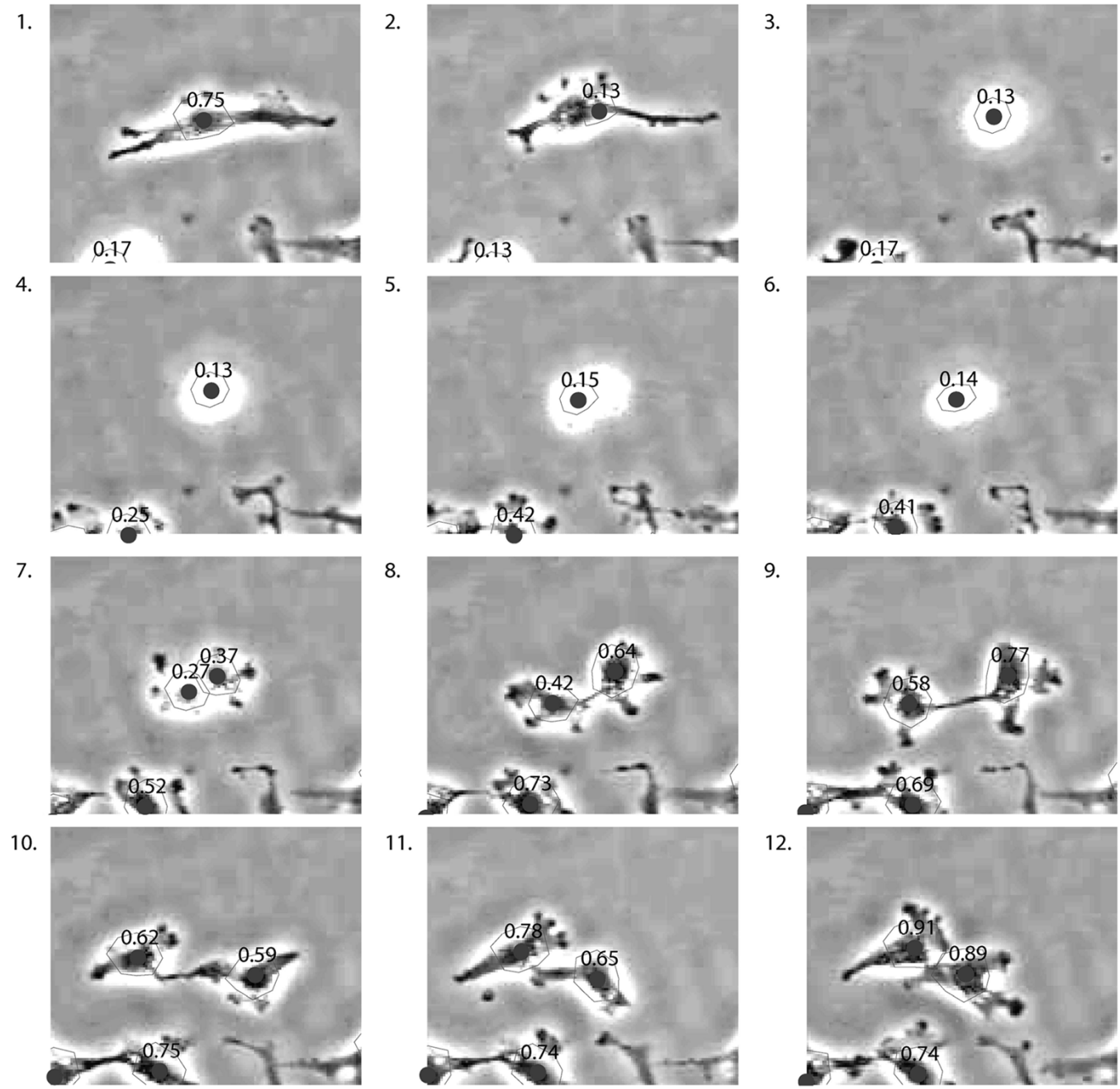

Fig. 4. Illustration of backward tracking during cell division (mitosis). Sequence of frames showing a cell entering the mitotic process (frame 3) until effective cell division (frames 5–7) resulting in two "daughter" cells (frames 8–12). This illustrates that during mitosis (frames 3–6) the inner (dark) part of a cell shrinks until few (or no) dark pixels remain visible. After division (frame 7), each "daughter" cell regains a dark-surrounded-by-halo shape (frames 8–12). To establish cell trajectories during mitosis, the tracking algorithm was used in the reverse direction (illustrated here from frame 12 to frame 1). Each frame illustrates the locations of the cell centroid determined by the algorithm together with the polygons defined by the $\mathbf{g}_{wi}$ mass centers (corresponding to the kernels attracted by white pixels, see Fig. 3). The numeric values correspond to the values of the α parameter [defined in (4)] controlling the adaptive model. These values indicate the variations in the cell sizes observed during a division.

accordingly (to maintain $r_{bi} = 0.5\, r_{wi}$). This adaptive model is well suited to track cells containing the targeted pattern, i.e., a dark area surrounded by a white halo.

However, in spite of their adaptive properties, this kind of model based on two nested kernels is not appropriate to track cells entering the mitotic process (i.e., cell division) during which the cells adopt a completely different pattern (i.e., a small bright disk with a very small inner darker part, see Fig. 4). We, therefore, consider a model with two different states: the normal state ("dark surrounded by white") and the mitotic state ("white surrounded by dark"). To take this mitotic state into account a third kernel, K_3, is considered by adding a trapeze with a constant thickness e at the external side of each A_{wi} triangle [see Fig. 3(b)]. The union of these trapezes forms kernel K_3 for which the mean-shift is computed on the inverted image as in the case of kernel K_2 (i.e., also attracted by the darkest pixels). The new cell position is computed with (1) with $i = 1$ to 3 and where the weight vector $(w_1, w_2, w_3)^{\mathrm{T}}$ may vary between

consecutive frames from a vector $\mathbf{W}$ corresponding to a normal state to $\mathbf{W}'$ corresponding to a mitotic state (the weights are kept constant during the mean-shift itself on a given frame). The resulting weight vector (labeled $\mathbf{W}^*$) for any cell being between these two states is given by (2) where α is a parameter extracted from the cell shape. As a cell in a mitotic phase appears to be shrinking (see Fig. 4), the interframe adaptive properties of the kernels in terms of the update of the r_{wi} values [see (3)] gives us an interesting parameter to identify cells entering the mitotic phase. Note that $\bar{d}$ (the mean distance from the cell centroid to the vertices of the polygon attached to bright pixels) is strongly correlated to cell size, in particular when the tracked cell adopts the mitotic pattern. Fig. 3(c) summarizes the underlying idea illustrating the variation of the α parameter [used in (2)] from a cell in the mitotic state to one in a normal state as a sigmoid function of $\bar{d}$

$$\alpha = \frac{1}{1 + e^{-s(\bar{d} - d^*)}} \tag{4}$$

where s is the slope of the model transition and d^* the threshold for transition. In our experiments the value chosen for d^* is 15 pixels that corresponds to the observed mean radius of cells in the mitotic state. The slope sets the steepness of the transition between both models (we use $s = 0.75$). Fig. 3(d) illustrates the 3-kernel based model applied on a cell in a "normal" state and the resulting polygon linking the $\mathbf{g}_{wi}$ mass centers. Fig. 3(e)–(g) shows the areas corresponding to kernel K_2 (attracted by the inner dark pixels), K_1 (attracted by the white halo pixels) and K_3 (attracted by the external dark pixels), respectively. The typical values used for the constant weight vectors, $\mathbf{W}$ and $\mathbf{W}'$, are given in Table I. While the contribution of K_2 is strongly weighted in $\mathbf{W}$ (normal cell model), the contribution of K_1 is reinforced in $\mathbf{W}'$ (mitotic cell model). A relatively slight contribution of K_3 is used in $\mathbf{W}'$ only.

E. Establishing Cell Trajectories Through Mitoses and Cell Crossing

In Section II-D, we detail how to adapt the combination of kernels in order to ensure the successful transition between the "normal" and the "mitosis" state of a cell (and inversely). Fig. 5 shows that the introduction of this adaptive feature is required to determine acceptable cell centroids. This figure illustrates the convergence paths generated by the algorithm when it is applied from different starting points located around the cell analyzed. These starting points were chosen to simulate different possible locations of the cell centroid which would be determined by the algorithm in the previous frame $(t-1)$ of the image sequence (and would initialize the convergence process in frame t). To indicate the direction of the convergence the final points are represented by squares (the starting points are, thus, at the other path extremities). The paths illustrated in Fig. 5 are obtained by applying the combined mean-shift process on the 3-kernel based model (described in Section II-D) on a cell in a "normal" state [Fig. 5(a) and (c)] and in a "mitotic" state [Fig. 5(b) and (d)], depending on whether the adaptive properties of the model are active [Fig. 5(a) and (d)] or inactivated [Fig. 5(b) and (c)]. Frames (a) and (d) evidence expected results. Note, on a cell in a "normal" state (a) each path converges to a point located in a darker area surrounded by white regions which is always inside the cell. These convergence points can, thus, be considered as "acceptable" cell centroid locations for the tracking process (compared to humanly located centroids in Section IV-A). On a cell in a "mitotic" state (d) all the paths converge to the center of the white disk characteristic of this state. In contrast, frames (b) and (c) show what happens if the adaptive features of the model are inactivated (i.e., the model is fixed before applying the mean-shift process). In fact, frame (b) exhibits the convergence paths obtained by using a model adapted for the cell shown in frame (a) (in a normal state) and fixed before being applied on the cell in mitosis. Similarly, frame (c) shows the convergence paths obtained by using a model adapted for the cell shown in frame (d) (in a mitotic state) and fixed before being applied on the cell in a normal state. These two experiments evidence that in both cases the process converges to points located near the cell boundary. These points cannot be considered as acceptable centroid locations because they would cause the loss of the cell in the following frames of the sequence.

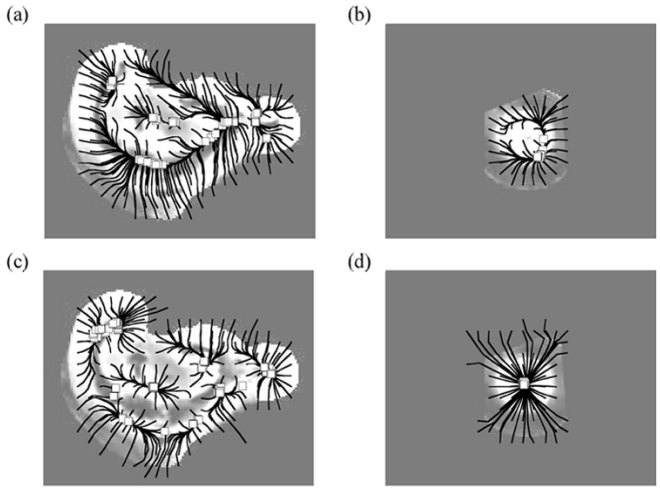

Fig. 5. Convergence paths generated by our combined means-shift model with [(a), (d)] active versus inactivated [(b), (c)] adaptive features. Illustration of the convergence paths resulting from the algorithm when it is applied from different starting points located around the cell analyzed. To indicate the direction of convergence, the ends of the paths are emphasized by square dots (the starting points are, thus, at the other path extremities). (b) Illustrates the results obtained on a cell in a mitotic state by using a fixed model previously adapted on the cell shown in (a) (i.e., with inactivated adaptive features). Conversely, (c) evidences what happens if a fixed model adapted to the cell shown in (d) is applied on a cell in a "normal" state (see text). (a) and (d) Results obtained with a model adapted to the respective cell states.

Another important point which has to be considered is that cell division increases the number of objects to track. It is interesting to connect cell trajectories during mitoses in order to establish the migration potential of a cell through its "descent," e.g., by measuring the distance covered by a cell and its successive cell generations (if the observation time allows it). This could interestingly characterize the potential of diffusion of a particular type of cells (e.g., cancer cells). The adaptive combination of kernels enables the successful transition to be carried out from one cell to one of its two daughters (through the mitosis pattern) and, thus, the connection of the two cell trajectories. However, using this method, only one daughter is taken

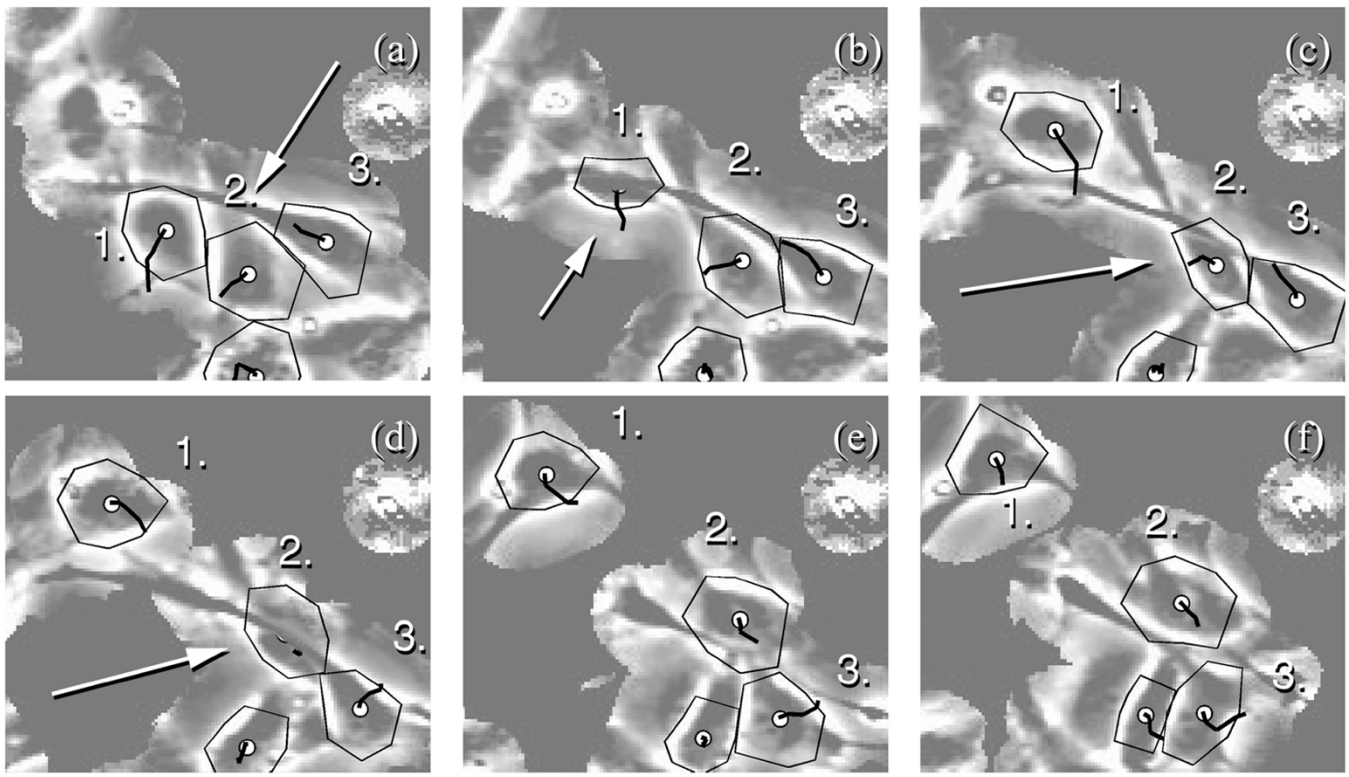

Fig. 6. This sequence of preprocessed images illustrates the tracking of four cells in close contact. Three of them (labeled 1, 2, and 3) present membrane protrusions crossing the trajectories of the other cells. For the sake of clarity, only 1 on 3 successive frames from the original sequences is shown together with the cell centroids (white dots), their associated polygons (corresponding to the kernels attracted by white pixels) and the cell paths (black lines) established by the tracking algorithm between the different frames. The beginning of each path illustrated in a frame corresponds to the associated cell centroid location (i.e., the path end) illustrated in the previous frame. (a) The crossing of membrane filopods extended by cells 2 and 3 (see the arrow). In (b) and (c), cell 1 crosses the membrane protrusion coming from cell 3. The same process is illustrated in the case of cell 2 in (c)–(f).

into account and tracked after each division (the second is lost). A complementary and easy way to establish trajectory connections between a cell and its two daughters is to track cells in the inverse time direction (i.e., from frame t to frame $(t-1)$). The mitotic event is very easy to detect in the inverse time direction because the centroids of two daughter cells progressively become close enough to be merged and the subsequent locations of both cells remain the same from the moment of division until the beginning of the sequence (in the reverse direction). Backward (or reverse) tracking, thus, enables both daughter cells to be taken into account in each cell division. Two trajectories are finally available including proper and common parts (the latter corresponds to the mother cell). Moreover, the detection of morphology changes described in the forward procedure (see Section II-D) is a very good way to avoid confusions between actual mitoses and cell trajectories presenting very near or overlapping parts. Fig. 4 illustrates the interest of the model adaptation and backward tracking from a dynamic point of view during a cell division. While the frames are numbered following the "natural" time, the tracking process is carried out in the reverse time direction (i.e., from frame 12 to 1). Each frame shows the polygons linking the $\mathbf{g}_{wi}$ mass centers together with the computed value of parameter α (see (4) in Section II-D) and the final cell centroid obtained after convergence. During reverse tracking, frames 12 to 6 illustrate the polygon contraction (characterized by decreasing α values) observed on two cells merging into a single one (in frame 6) and the inverse process occurring in frames 2 and 1 (with progressively larger α values). Frame 12 to 7 also illustrate the ability of the (backtrack) algorithm to correctly follow two cells which remain close to one another and present overlapping halos. Overlapping may also occur when one cell crosses another cell trajectory (e.g., when it climbs on a membrane protrusion of another cell). Fig. 6 illustrates that our tracking algorithm is able to follow cells in such situations. It shows 4 cells in close contact, their associated polygons (defined by the $\mathbf{g}_{wi}$ mass centers) and centroids (white dots) and their linkings across frames (black paths) which are automatically determined by our algorithm on a sequence of frames (a) to (f). The cells labeled 1, 2, and 3 in Fig. 6 exhibit membrane protrusions which cross another cell trajectory. While in frame A cell 3 extends a long membrane protrusion (see the arrow) over the two other cells (1 and 2), in Fig. 6(b) and (c) cell 1 moves below this membrane protrusion toward another location [see Fig. 6(c)]. As illustrated the algorithm is able to follow cell 1 during this crossing. The same process is illustrated in frames (c) to (f) in the case of cell 2 (see arrows) which also moves below the membrane protrusion extended by cell 3 toward another location. Again, the tracking algorithm does not lose cell 2 during its movement. Of course, in some cases the model associated to a cell converges to another close cell during the mean-shift process, causing an incorrect inter-frame association. The occurrence of these tracking errors is evaluated in Section IV-A.

It should be noted that the results illustrated in Figs. 4, 5, and 6 concern images preprocessed as detailed in Section III-C.

III. Application Features

A. Acquisition

Cell cultures in Falcon plastic dishes maintained at 37 °C were observed and recorded automatically every 4 min by means of the device described previously [12], [13]. Briefly, the images were acquired under a phase-contrast microscope (Olympus, model IX50, magnification ratio 10:1), with a charge-coupled device video camera (Hitachi Denshi, model KP-M1E/K-S10) coupled with an acquisition board (32-bits Matrix Vision PC-GRAB-GI frame grabber). The image dimensions are 700×500 pixels (with a pixel resolution of 0.92 μm at the magnification ratio abovementioned) discretized on 256 gray levels (8 bits/pixel). The uncompressed images were stored on a computer hard disk.

B. Manual Initialization

As the sole interactive part of the algorithm, the human operator is asked to manually select the cells to be tracked on either the first frame (forward tracking) or the last frame (backward tracking) of the sequence by marking them with the computer mouse. To allow the operator to execute this task quickly, the tracking algorithm described in Section II is already used to automatically adjust the mark position at the cell centroid position. In Section II-E we show that our tracking algorithm exhibits paths converging sharply to a small number of regions reduced in size and which correspond to almost acceptable cell centroid locations, i.e., situated inside the cell (in a relatively central region). The distances between centroid locations automatically and manually determined are illustrated in Section IV-A.

C. Preprocessing

As we want to be able to observe cell migration during a long period of time (we carried out experiments lasting 72 h, cf. [12] and [13]), we cannot use high intensity illumination that could disturb living material under study. So the images acquired generally have low contrast. This is why we apply a preprocessing step to enhance the image contrast and prevent lighting problems (such as vignetting and illumination changes). The preprocessing consists in first roughly detecting the image background, i.e., the part of the image including no cell. The background is almost continuous compared to the cell areas which are characterized by the presence of many borders. We extract the border information from the image using a gray level morphological gradient [23] with a circular structuring element of radius equal to 15 pixels (equivalent to the smallest cell size encountered in our various experiments). The resulting gradient image is thresholded at value 50 (in the 8-bit scale used). Fig. 7(a) and (b) illustrates a typical cell culture image and the corresponding thresholded gradient (binary) image used as the background mask, respectively.

Contrast enhancement and illumination correction is achieved using a local equalization described as a local enhancement in [24]. In our version, the new equalized value is computed for each pixel on the basis of the gray level distribution of the circular neighborhood around the pixel. The radius used is fixed to 20 pixels and ensures a good contrast between the inner part of the cells (darker areas) and the surrounding region (brighter areas). As illustrated in Fig. 7(c) this kind of local equalization [applied on the image shown in Fig. 7(a)] produces a high level of contrast and a uniform gray level distribution across the image. To remove the amplified background noise, the image is masked (i.e., multiplied) by the previously computed background mask, as shown in Fig. 7(d).

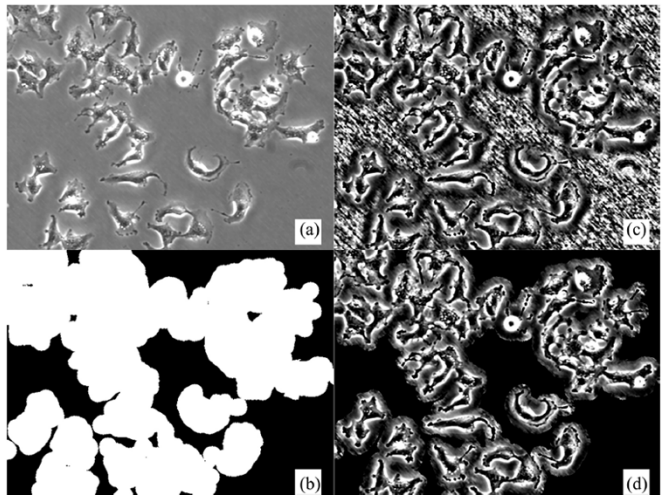

Fig. 7. Illustrations of the preprocessing steps used in our application (see text).

Thresholding, equalizing, and masking are applied to the complete sequence.

It should be noted that several constant values have been introduced in the different preprocessing steps (summarized in Table I). Of these constants, the two radius values are scale-dependent. In Section IV-C we investigate the sensitivity to these different parameters.

D. Cell Trajectory Features

As defined in our previous works [12], [13], for each cell trajectory, we computed the average speed (AS), which is the mean distance covered by a cell per time unit and the Maximum Relative Distance to Origin (MRDO) feature. The latter feature refers to the greatest linear distance between the original position of the cell and the farthest position reached by the cell in its trajectory. MRDO is in fact the maximal distance normalized by the observation time for the cell analyzed (to be able to compare cell trajectories corresponding to different observation times). In contrast with AS, MRDO is able to distinguish between cell trajectories constituted of many small movements (around the original cell location) and those presenting few large displacements, as detailed in [13]. In the present paper, we extended the MRDO feature to two others, labeled HULL and MAXDIST. The HULL feature is based on the convex hull polygon constructed on all the positions occupied by a cell during its displacement; this is the smallest convex set that includes all the points of the cell trajectory. The HULL feature is the area (pixel^2) of the convex hull (i.e., the area covered by the cell trajectory) normalized by the observation time of the cell analyzed (similarly to MRDO). The MAXDIST is the maximum distance between two points of the cell trajectory (whatever are these points), also normalized by the observation time of the cell. MAXDIST is, thus, a generalization of MRDO, freed of the first cell position (taken

as reference in MRDO). This also corresponds to the maximum distance between two points of the convex hull.

IV. Algorithm Validation and Robustness Study

A. Automatic Versus Human Cell Tracking

Our automatic tracking process was compared to that achieved by a human operator on image sequences of A549 cells (illustrated in Fig. 1(f) and also used in the application reported in Section V) filmed during 24 h (1 frame acquired every 4 min). This was carried out as follows. Each cell in three different image sequences (360 frames/sequence) was automatically and manually tracked in the backward direction. In order to make the manual task less tedious, the operator used an interface that showed a given cell in a close up display every 10th frame. For each cell, the successive centroid locations marked by the operator were then interpolated using line segments to determine the complete trajectory. The locations of all the cells marked by the human operator in the last frame were used to initiate the backward automatic tracking process. This experiment is based on 280 supervised cell trajectories (i.e., between 90 and 100 trajectories per sequence). For each cell trajectory we computed the average distance (in pixels) at each time step between the supervised (and interpolated) cell locations and those computed by the algorithm. Fig. 8(a) shows the distribution of these distances (means $\pm$ standard errors computed on the 280 trajectories analyzed) according to time. As the automatic tracking was carried out backward, a slight and progressive increase in distance occurs in the reverse time direction (from frame 360 to 1) and probably results from error accumulation. The final mean distance (on frame 1) is 15.22 pixels $(\mathrm{SEM} = 1.25)$. This distance is near to the average radius of cells during mitosis, while the typical radius of cells (in a normal state) is around 25 pixels. This indicates that the location errors are small compared to the size of the cells. Furthermore, it can be noted that the interpolation applied on the manually marked cells might introduce a certain error rate according to the actual cell locations and pessimistically biases the distances reported here. Fig. 8(b) displays the percentages of cells successfully tracked by the algorithm according to time. To simplify this evaluation a cell was considered as definitively "lost" by the tracking algorithm the first time that the distance between the supervised and automatic centroid locations exceeded a given threshold value (we observed that sometimes the algorithm loses and then recovers a cell). Each curve in Fig. 8(b) corresponds to a particular threshold value (25, 50, 75, or 100 pixels). As expected the percentages of lost cells increased with time (in the backward direction). However, only 10% of cells can be considered as lost at the end of the automatic tracking (i.e., after 24 h) in the case of a threshold value fixed to 50 pixels. This value (which equals twice the mean radius of a cell in its normal state), thus, corresponds to the distance to the possible centroid location of another cell which would be very close (i.e., adjacent) to the tracked cell. We indeed observed that a large majority of these cases of cell losses correspond to an incorrect inter-frame association carried out by the mean-shift process.

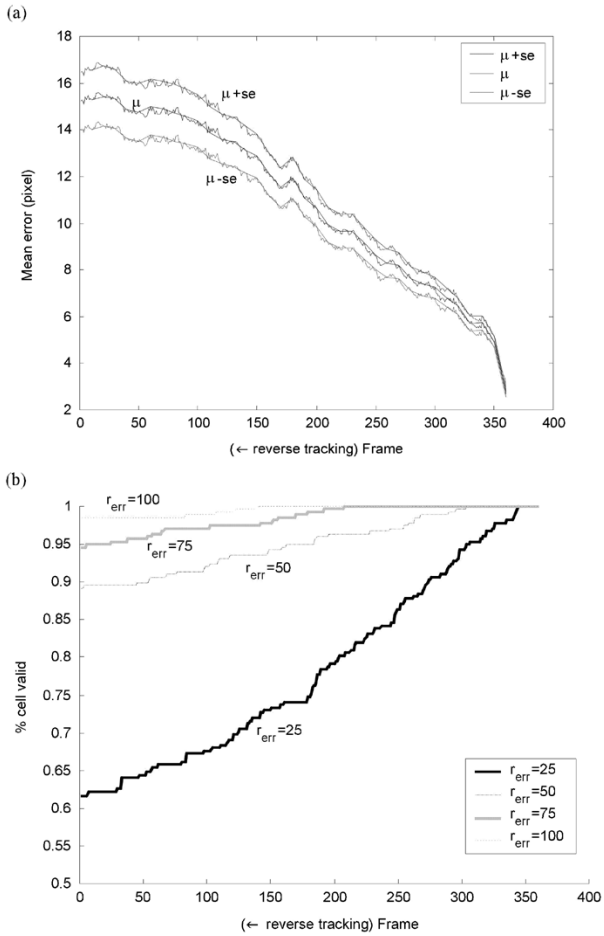

Fig. 8. Validation of the automatic tracking procedure by a human operator. Comparison between cell trajectories manually tracked by a human operator and those automatically generated by our tracking procedure used in the backward direction (from frame 360 to frame 1 indicated on the horizontal axis). The data, based on a total of 280 trajectories, show (a) the mean distances between the manually and the automatically tracked trajectories, and (b) the percentages of cells successfully tracked by the algorithm, determined according to a fixed threshold of the distance to the supervised trajectories. While the data in (a) are displayed as mean distances $-$ their standard errors (in pixels), the different curves in (b) correspond to different threshold values (25, 50, 75, and 100 pixels) for which the distances to the supervised trajectories are considered too large and the cells labeled as "lost."

B. Sensitivity to Algorithm Parameters

We evaluated the model sensitivity to the parameters (for which typical values are given in Table I) by comparing the tracking results obtained with a series of several modified parameter sets. For each set, we perturbed one parameter value in a certain range. The sensitivity was evaluated in two different and complementary ways. First, we compared the automatic and supervised tracking results by means of the error measurements introduced in Section IV-A (the mean errors and the percentages of the lost cells computed using threshold values of 50 and 75 pixels). Second, we evaluated the different features characterizing the cell trajectories introduced in Section III-D, and analyzed their possible variations.

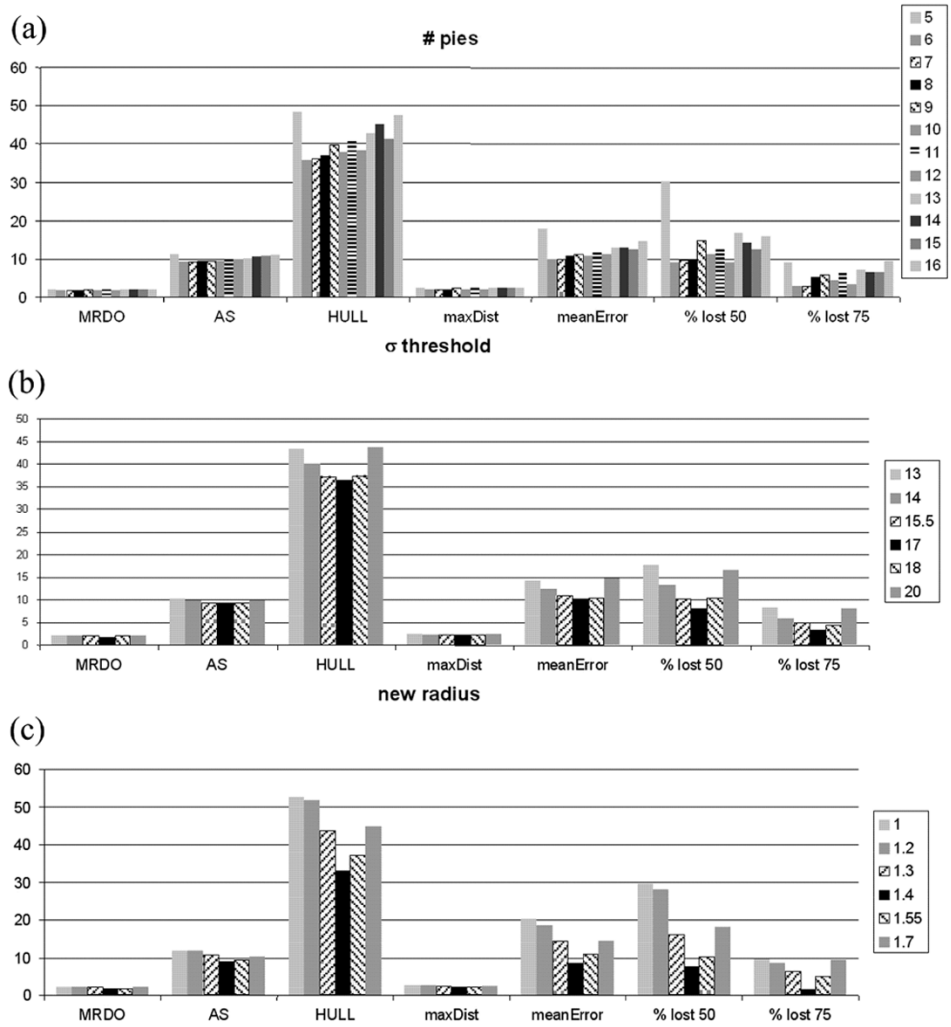

Fig. 9. Sensitivity to algorithm's parameters. The parameters analyzed are (a) the number of pies used in the mean-shift kernels (see Fig. 3). (b) Threshold d^* of the sigmoid function used in the model transition [see (4)]. (c) factor k of model expansion [see (3)]. The different parameter values considered are indicated in each frame. The variations observed are reported in terms of the trajectory features introduced in Section III-D (MRDO, AS, HULL, and MAXDIST) and the error measurements illustrated in Fig. 8, i.e., the mean errors (corresponding to the mean distances to the supervised trajectories) and the percentages of the lost cells computed using 50 and 75 pixels as threshold values (labeled %''lost 50 and % lost 75). While the values of MRDO, AS, and MAXDIST are expressed in pixel/h, the HULL ones are in pixel^2/h.

Fig. 9 illustrates the results concerning tracking sensitivity to three important parameters controlling our algorithm, i.e., the number of pies used in our kernels $(\text{default} = 8)$, threshold d^* of the sigmoid function used in the model transition (see (4); $\text{default} = 15.5$) and factor k of model expansion (see (3); $\text{default} = 1.55$). With respect to the kernel geometry, Fig. 9(a) shows the results obtained when the number of pies varies from 5 to 16. The mean error and the percentages of lost cells are very large if the number of pies is lower than 6, probably due to a lack of flexibility of the model. Some slight fluctuations also appear when the number of pies becomes large, e.g., increase in the percentage of lost cells (considering a threshold of 50) if more than 8 pies are used. This increase (paralleled by a progressive increase in the mean error) could be due to the fact that by increasing the number of pies, we decrease the number of relevant pixels (black or white) inside each pie, thus making the model more sensitive to noise. The choice of the number of pies, thus, has to establish a tradeoff between model flexibility (i.e., the ability to track deformable objects) and robustness to noise (which occurs when the pies cover small areas). Concerning the trajectory features, while the distance-based features (e.g., MRDO and MAXDIST) appear as being statistically very stable (even in the case of 6 pies), the HULL feature is more sensitive (as expected for an area measurement depending on each of the cell positions), paralleling the profile of the mean error measurement. The AS feature (depending on the total trajectory length) exhibits an intermediary profile.

Fig. 9(b) similarly investigates the sensitivity to the sigmoid threshold (d^*) with values between 13 and 20, and shows that very similar results are obtained for values between 15.5 and 18 (minimizing the errors). These values correspond to the radii of cells in a mitotic state.

Fig. 9(c) concerns the sensitivity to factor k with values between 1 (i.e., no expansion) and 2 (i.e., double expansion). Comparatively to the results described above on the other algorithm parameters studied, Fig. 9(c) evidences a higher level of sensi-

tivity of the results (in terms of errors essentially) according to variations in k values. The errors are minimal for values around 1.40. Again, the MRDO and MAXDIS features appear to be statistically insensitive to these variations.

We also tested sensitivity to other algorithm parameters such as the sigmoid slope for model transition [see (4)], the anisotropy level introduced by factor β in (3), as well as the weights used in the kernel combination [see (1)]. We did not observe particular sensitivity to these parameters around the default values $(\pm 25\%)$ mentioned in Table I (data not shown).

C. Sensitivity to Preprocessing Parameters

The preprocessing phase is based on three parameters which are the radius of the border detection, the threshold of the gradient value, and the radius of the local contrast enhancement (see Section III-C). To test the method's sensitivity to these parameters, we preprocessed two series of images (one based on a cell in a mitotic state and the other on a cell in a normal state) with different preprocessing parameter values, such as a gradient radius varying from 5 to 30 pixels, a background threshold from 10 to 50 and an equalization radius from 5 to 30 pixels. In each case, we applied the tracking algorithm from different starting points located around each cell analyzed (as already illustrated in Fig. 5). We then tested if the position of the model (i.e., the cell centroid determined by the algorithm) converged into a region of acceptable cell centroid locations (determined by a human expert). Fig. 10(a)–(c) shows the percentage of satisfactory centroid locations found for each series of preprocessed images according to the different values of the three parameters analyzed. These data show that the results relative to the gradient radius and background threshold are very stable [Fig. 10(a)–(b)]. In contrast, the equalization radius seems to have more effects on the results, particularly in the case of a mitotic cell [Fig. 10(c)]. However, these variations stabilize for equalization radii larger than 14.

This can be explained by the fact that a mitotic cell is reduced in size (as compared to a normal cell) and is, thus, more sensitive to the noise introduced by the enlarged image background resulting from a decrease in the equalization radius.

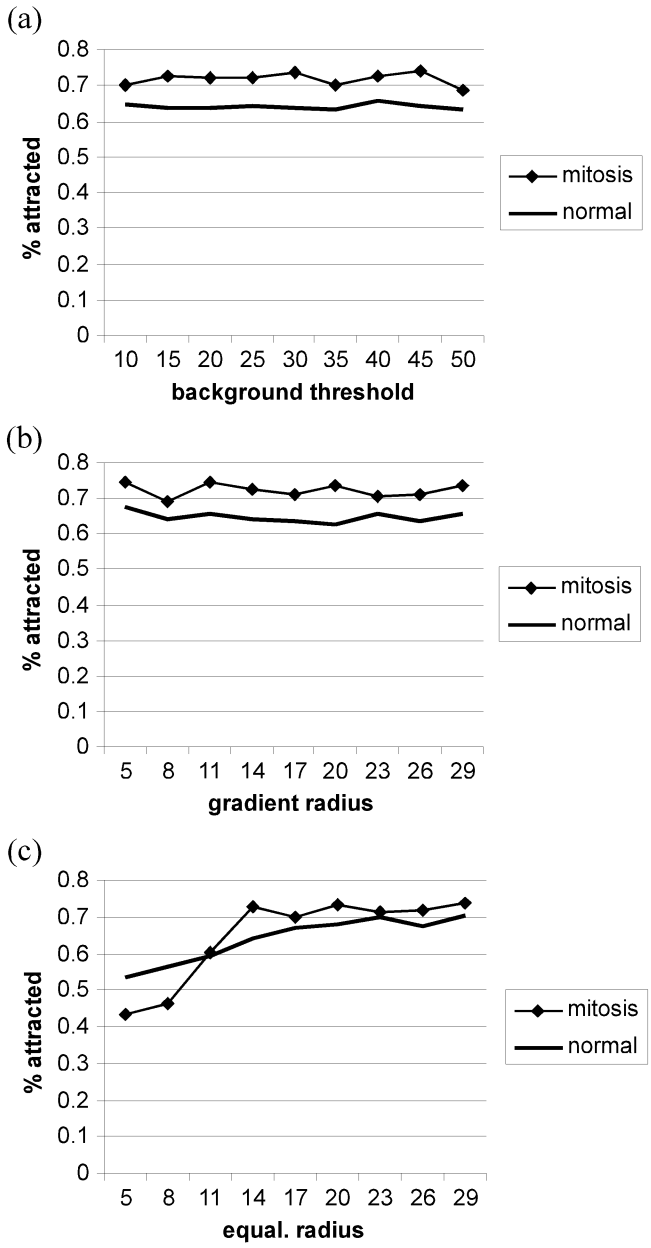

Fig. 10. Sensitivity to preprocessing parameters. The parameters analyzed (and detailed in Section III-C) are the gradient radius (b), the background threshold (a), and the equalization radius (c). The effects were evaluated on two series of images, one based on a cell in a mitotic state and the other on a cell in a normal state. Applying the tracking algorithm from different starting points located around each cell analyzed (as illustrated in Fig. 5), we tested if the positions of the model (i.e., the cell centroids located by the algorithm) converged into a region of acceptable cell centroid locations given by a human expert. (a)–(c) shows the percentage of satisfactory centroid locations (found for each series of preprocessed images) according to the different values of the three parameters analyzed.

D. Robustness Against Defocusing

One typical problem that occurs during long sequences (more than 1 day), is the loss of focus due to evaporation of the substrate, mechanical shift of the microscope, etc. In the present study, no autofocus device was considered in the acquisition setup. We were, thus, interested in the robustness of the algorithm against small change in the Z position of the sample. Due to the general principles of the method, small changes of the focus only affect high spatial frequency details of the image (i.e., texture of the background and intracellular refractive objects). To corroborate this assumption we generated synthetic blurred versions of an acquisition sequence by a spatial Gaussian convolution kernel of increasing standard deviation (σ, cf. [24]). Five blurred sequences (with $\sigma = 1, 3, 5, 7$, or 9) were generated from a sequence for which 49 manually supervised trajectories were available. The blurred and supervised sequences were compared with the evaluation method described in Section IV-A. This is illustrated in Fig. 11(a) which shows different curves (corresponding to increasing σ) plotting (according to time) the mean distances between the (linearly interpolated) supervised trajectories and the automatically generated ones using backward tracking. Of course, the tracking process lost its efficiency when the blur level increased too much [Fig. 11(a)].

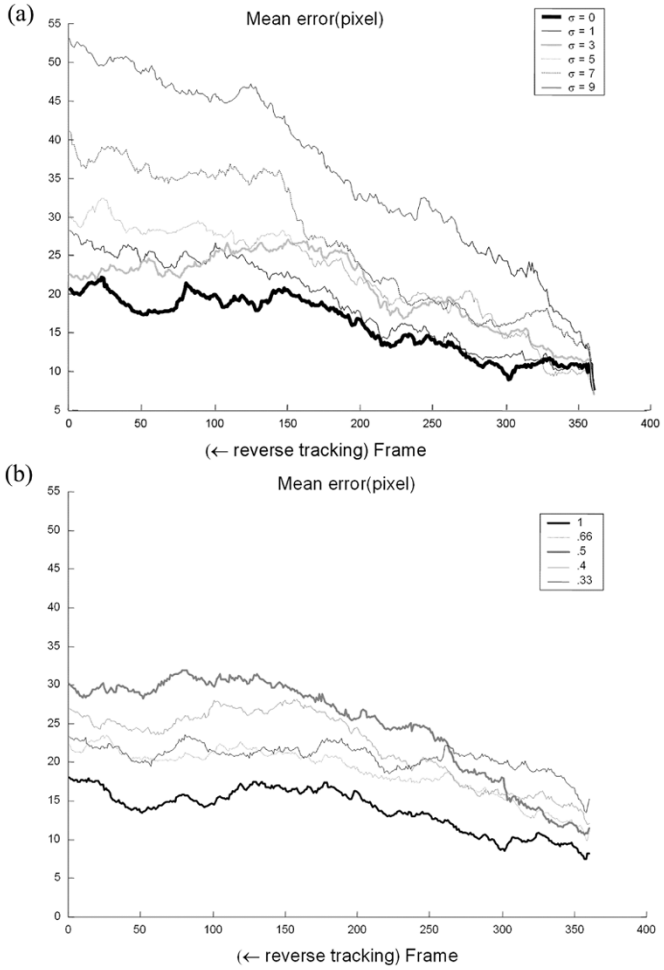

Fig. 11. Robustness of the tracking process with respect to loss of focus and image resolution. (a) Distribution over time of the mean distances measured between 49 supervised cell tracks and those established automatically in the presence of different blurring levels. (b) Distribution over time of the mean distances measured between 49 supervised cell tracks and those established automatically in the case of different levels of image resolution decrease. The automatic tracking was carried out in the backward direction (i.e., from frame 360 to frame 1 indicated on the horizontal axis).

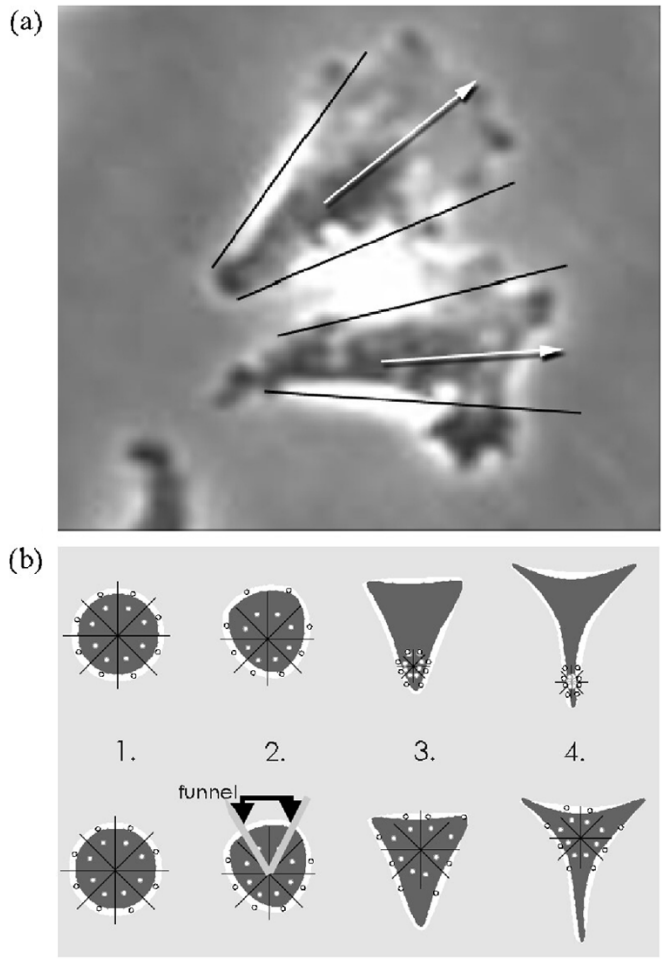

Fig. 12. Funnel shape displacement. (a) Example of migrating cells presenting a funnel shape. (b) Top: Progressive shift of the kernels in the absence of funnel detection and correction. Bottom: Principle of funnel detection (frame 2) and correction of the kernel shifts accordingly. The kernels are located by the mass centers $\mathbf{g}_{bi}$ and $\mathbf{g}_{wi}$.

However, low blur levels did not significantly affect the performances. An autofocus device does not, therefore, seem essential in our application.

E. Robustness Against Change in Resolution

In order to evaluate the effects of image resolution on the tracking results we artificially built a degraded version of the reference sequence by subsampling it (factors used: 0.666, 0.5, 0.4, and 0.333). The scale-dependent algorithm parameters (see Table I) were rescaled accordingly. The supervised and subsampled sequence tracking were compared and the mean distances computed (after rescaling each subsampled track back to the supervision scale). Similarly to Fig. 11(a), Fig. 11(b) shows that the tracking performances remain acceptable even if acquisition is half the size.

F. Handling Funnel

One limitation of our algorithm concerns the tracking of rapidly moving cells which present a funnel-shaped displacement, as illustrated in Fig. 12(a) (where each arrow indicates the cell movement direction). This cell shape deformation showing a large membrane protrusion in front of the cell is the result of a polarization process which occurs in migrating cells [25]. We observed that the algorithm lost the cell during tracking if the cell deformation was strong [as schematically illustrated in Fig. 12(b)] and associated with a high displacement speed. The problem is due to the presence of an excess of bright pixels (halo) in the narrow part of the funnel. As a consequence, kernel K_1, which is attracted by bright pixels (see Section II), and its gravity center $(\mathbf{m}_1)$ are shifted to the narrow part of the funnel [see the top of Fig. 12(b)]. Due to the kernel linkage, the combined iterative process [(1) in Section II-C] consequently displaces the cell centroid toward this funnel area, i.e., in the opposite direction to the expected cell displacement. Using the representation introduced in Fig. 3, the top of Fig. 12(b) schematizes this progressive shift by showing the successive locations of the local mass centers ($\mathbf{g}_{wi}$ and $\mathbf{g}_{bi}$) relative to the triangles constituting the two nested kernels, K_1 (attracted by the bright pixels) and K_2 (attracted by the internal dark pixels).

To avoid this shift problem, we designed a funnel indicator based on the analysis of the distances between two consecutive

local mass centers, $\mathbf{g}_{wi}$ and $\mathbf{g}_{w(i+1)}$. A funnel-shaped displacement is characterized by the fact that some of these distances are relatively large, indicating the presence of membrane protrusions [see frame no. 2 in Fig. 12(b)]. The funnel indicator, thus, only checks if those distances are greater than a certain proportion (e.g., 1.2) of the average distance mean (meaning that there are rather different distances between the $\mathbf{g}_{wi}$ centers). If it is the case, we determine the direction given by the mediating line to the segment joining the two most distant mass centers. This direction is indicative of the polarization axis of the cell [Fig. 12(b)]. To attenuate the centroid shift a small displacement is added in the direction of this median line. The bottom of Fig. 12(b) illustrates the effects on the cell centroid location of the corrections so introduced.

It should be noted that a large number of experiments were successfully carried out without this algorithm adjustment. We observed that funnel-shaped cell displacement is more marked (and, thus, requires the adjustment described in this section) in certain specific cell culture conditions, in particular in the case of cells growing in Dunn Chamber [7], [8] (data not shown).

G. Computation Time

The computation cost of the complete tracking procedure is directly proportional to the number of tracked cells. We evaluated that the tracking of 100 simultaneous trajectories (a common situation in reverse tracking) requires about 0.5 s/image on a Pentium IV computer. To this must be added 2–3 s/image for the preprocessing steps, i.e., the complete procedure takes less than 4 s/image.

V. Application to Anti-Motility Drug Testing

A. Experimental Setup

We applied our cell tracking algorithm to a series of *in vitro* experiments aiming to test the effects of cytochalasin-D on the migration of A549 colic tumor cells [illustrated in Fig. 1(f)]. It is known that cell motility requires a highly dynamic actin cytoskeleton with a rapid actin filament assembly and disassembly [25]. Cytochalasin-D, which is known as an inhibitor of actin polymerization, acts on these dynamics and is, thus, suspected to affect cell motility [26]. Cell cultures in Falcon plastic dishes maintained at 37 °C were observed and recorded during 24 hrs as described in Section III-A. We investigated the motility behavior of A549 cells in 4 experimental conditions. The cells were either left untreated (control), or treated with cytochalasin-D at 3 decreasing concentrations ($10^{-7}, 10^{-8}$, and 10^{-9} M). These concentrations were noncytotoxic (i.e., without significant effects on the A549 cell growth level, data not shown). Each condition was run in triplicate. The image sequences were processed according to the (backward) tracking algorithm described in Section II (with the default parameter values indicated in Table I) after the preprocessing steps described in Section III-C and the manual initialization made on the last frame of each sequence (see Section III-B). In each experimental condition cell motility was characterized by means of the different trajectory features introduced in Section III-D (i.e., MRDO, AS, HULL, and MAXDIST). The significance of the cytochalasin effects was tested by means of the nonparametric Wilcoxon and Mann-Withney tests.

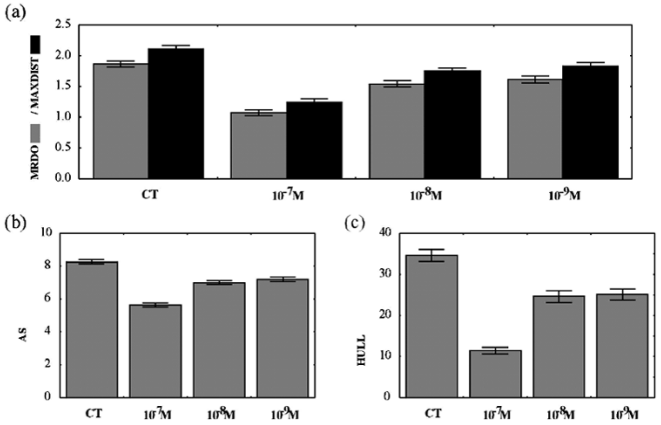

Fig. 13. Effects of cytochalasin-D on A549 cell motility. The effects of three decreasing concentrations of cytochalasin-D ($10^{-7}, 10^{-8}$, and 10^{-9} M) were evaluated on A549 cells observed during 24 hours ($\mathrm{CT} = \mathrm{control}$, i.e., untreated cells). The motility features analyzed are the different trajectory features introduced in Section III-D, i.e., MAXDIST and MRDO (a), AS (b), and HULL (c). The data show the means ± SE in each condition.

B. Tracking Results

By pooling the 3 image sequences recorded for each experimental condition, we finally analyzed 274 cell trajectories in control and 177, 297, and 199 trajectories under $10^{-7}, 10^{-8}$, and 10^{-9} M of cytochalasin-D respectively. Fig. 13 illustrates the variations observed for each motility feature as compared to the untreated cells (control). Cytochalasin-D affected each feature in a dose-dependant way. Indeed, while a clear decrease was observed (from 30% for AS to 70% for HULL) in presence of the highest drug concentration, more reduced effects were exhibited under the other conditions. However, statistical tests confirmed the significance of all these effects as compared to control $(\mathrm{p} < 0.001)$. As evidenced in Fig. 13 the two lowest concentrations (conditions B and C) exerted similar effects $(\mathrm{p} > 0.05)$ on the different features analyzed. We can, thus, conclude that cytochalasin-D is able to significantly inhibit A549 cell motility. These experiments are included in a study carried out at the Laboratory of Toxicology (U.L.B., Brussels, Belgium), which study aims to characterize the effects on cancer cell migration of different drugs targeting actin (unpublished data).

VI. Conclusion and Future Works

We have presented a (quasi-)automatic method to track many cells through large image sequences covering relatively long periods of time (such as 1 to 3 days). This enables cell responses to physiological stimuli or culture conditions near biological reality (e.g., different matrix supports) to be analyzed. The proposed method is able to track cells from image sequences acquired under standard phase-contrast video microscopy. This avoids the use of luminescent cell markers and multiple cell irradiation (consequently required for image acquisition) which might influence and modify cell behavior. Furthermore, the use of luminescent probes strongly limits the period of observation because of fading, and, thus, only quick cell responses (to a strong stimulus, like a drug) can be screened.

The proposed method is based on the mean-shift principles and introduces the use of adaptive combinations of linked kernels. This approach allows the detection of various gray-level configurations and the transition between them. We demonstrated its ability to track a large number of cells in culture in the presence of cell divisions. As the method does not focus on cell boundary detection, it shows robustness with respect to variability in cell morphologies (between different cell cultures), cell overlaps, and dynamical changes in cell shape during cell migration. Furthermore, the running time of the software is very short, allowing improved possibilities in acquisition frequency and, consequently, improved descriptions of complex cell trajectories presenting quick displacements and strong cell shape deformations.

The present method has also some limitations which could be overcome by additional developments.

- As in other related works (e.g., [5]) the method requires manual initialization of the cell centroids on the first (or last) frame of the sequence. It is, thus, unable to handle new cells entering into the analyzed microscope field later. An automatic initialization scheme should be introduced by adding kernel-based models at the borders of the field, "awaiting" the entry of new cells to be active.
- As the method is directed toward a model-matching approach without any segmentation aim, no precise information is available on the cell boundaries and shapes. If this kind of information is required for analyzing features other than cell trajectories, postprocessing steps could be added, such as the use of active contours or level sets initialized on the cell centroids detected by the mean-shift based method.
- In the present study, no temporal filtering or time-dependent feature has been used. It could be interesting to extend the spatially combined model described in this paper, into a space-time-coupled model by linking the mean-shift process on successive frames (similarly to the spatial kernel linkage described in this paper).
- Finally, as the method shows robustness against defocusing, we are now considering the possibility of tracking living cells embedded into a 3-D substrate.

ACKNOWLEDGMENT

The authors would like to thank C. Verbeek for his help and patience with the tedious task of manual tracking.

REFERENCES

[1] G. Liao, T. Nagasaki, and G. G. Gundersen, "Low concentrations of nocodazole interfere with fibroblast locomotion without significantly affecting microtubule level: Implications for the role of dynamic microtubules in cell locomotion," *J. Cell Sci.*, vol. 108, pp. 3473–3483, 1995.

[2] C. Hayot, S. Farinelle, R. De Decker, C. Decaestecker, F. Darro, R. Kiss, and M. Van Damme, "*In vitro* pharmacological characterizations of the anti-angiogenic and anti-tumor cell migration properties mediated by microtubule-affecting drugs, with special emphasis on the organization of the actin cytoskeleton," *Int. J. Oncol.*, vol. 21, pp. 417–425, 2002.

[3] B. Joseph, F. Darro, A. Behard, B. Lesur, F. Collignon, C. Decaestecker, A. Frydman, G. Guillaumet, and R. Kiss, "3-Aryl-2-quinolone derivatives: Synthesis and characterization of *in vitro* and *in vivo* antitumor effects with emphasis on a new therapeutical target connected with cell migration," *J. Med. Chem.*, vol. 45, pp. 2543–2555, 2002.

[4] F. Lefranc, I. Camby, N. Belot, E. Bruyneel, C. Chaboteaux, J. Brotchi, M. Mareel, I. Salmon, and R. Kiss, "Gastrin significantly modifies the migratory abilities of experimental glioma cells," *Lab. Invest.*, vol. 82, pp. 1241–1252, 2002.

[5] C. Zimmer, E. Labruyere, V. Meas-Yedid, N. Guillen, and J. C. Olivo-Marin, "Segmentation and tracking of migrating cells in video microscopy with parametric active contours: A tool for cell-based drug testing," *IEEE Trans. Med. Imag.*, vol. 21, no. 10, pp. 1212–1221, Oct. 2002.

[6] D. W. Capson, R. A. Maludzinski, and I. A. Feuerstein, "Microcomputer-based interactive tracking of blood cells at biomaterial surfaces," *IEEE Trans. Biomed. Eng.*, vol. 36, no. 8, pp. 860–864, Aug. 1989.

[7] S. E. Webb, J. W. Pollard, and G. E. Jones, "Direct observation and quantification of macrophage chemoattraction to the growth factor CSF-1," *J. Cell Sci.*, vol. 109, pp. 793–803, 1996.

[8] W. E. Allen, D. Zicha, A. J. Ridley, and G. E. Jones, "A role for Cdc42 in macrophage chemotaxis," *J. Cell Biol.*, vol. 141, pp. 1147–1157, 1998.

[9] A. Czirok, K. Schlett, E. Madarasz, and T. Vicsek, "Exponential distribution of locomotion activity in cell cultures," *Phys. Rev. Lett.*, vol. 81, pp. 3038–3041, 1998.

[10] D. Dormann, T. Libotte, C. J. Weijer, and T. Bretschneider, "Simultaneous quantification of cell motility and protein-membrane-association using active contours," *Cell Motil. Cytoskeleton*, vol. 52, pp. 221–230, 2002.

[11] K. Wu, D. Gauthier, and M. D. Levine, "Live cell image segmentation," *IEEE Trans. Biomed. Eng.*, vol. 42, no. 1, pp. 1–12, Jan. 1995.

[12] C. De Hauwer, I. Camby, F. Darro, I. Migeotte, C. Decaestecker, C. Verbeek, A. Danguy, J.-L. Pasteels, J. Brotchi, I. Salmon, P. Van Ham, and R. Kiss, "Gastrin inhibits motility, decreases cell death levels and increases proliferation in human glioblastoma cell lines," *J. Neurobiol.*, vol. 37, pp. 373–382, 1998.

[13] C. De Hauwer, F. Darro, I. Camby, R. Kiss, P. Van Ham, and C. Decaesteker, "*In vitro* motility evaluation of aggregated cancer cells by means of automatic image processing," *Cytometry*, vol. 36, pp. 1–10, 1999.

[14] F. Leymarie and M. D. Levine, "Tracking deformable objects in the plane using an active contour model," *IEEE Trans. Pattern Anal. Mach. Intell.*, vol. 15, no. 6, pp. 617–634, Jun. 1993.

[15] N. Ray, S. T. Acton, and K. Ley, "Tracking leukocytes *in vivo* with shape and size constrained active contours," *IEEE Trans. Med. Imag.*, vol. 21, no. 10, pp. 1222–1235, Oct. 2002.

[16] F. Andre, B. Janssens, E. Bruyneel, F. van Roy, C. Gespach, M. Mareel, and M. Bracke, "Alpha-catenin is required for IGF-I-induced cellular migration but not invasion in human colonic cancer cells," *Oncogene*, vol. 23, pp. 1177–1186, 2004.

[17] M. J. Brown and L. W. Loew, "Electric field-directed fibroblast locomotion involves cell surface molecular reorganization and is calcium dependent," *J. Cell Biol.*, vol. 127, pp. 117–128, 1994.

[18] J. A. Sethian, *Level Set Methods and Fast Marching Methods*, Cambridge, U.K.: Cambridge Univ. Press, 1999.

[19] D. Comaniciu, V. Ramesh, and P. Meer, "Kernel-based object tracking," *IEEE Trans. Pattern Anal. Mach. Intell.*, vol. 25, no. 5, pp. 564–575, May 2003.

[20] R. Collins, "Mean-shift blob tracking through scale space," in *Proc. Computer Vision and Pattern Recognition (CVPR'03)*, 2003, pp. 234–241.

[21] H. Tek, D. Comaniciu, and J. Williams, "Vessel detection by mean-shift based ray propagation," in *Proc. IEEE Workshop Mathematical Methods in Biomedical Image Analysis*, 2001, pp. 228–235.

[22] Y. Cheng, "Mean shift, mode seeking, and clustering," *IEEE Trans. Pattern Anal. Mach. Intell.*, vol. 17, no. 8, pp. 790–799, Aug. 1995.

[23] H. J. A. M. Heijmans and L. Vincent, "Graph morphology in image analysis," in *Mathematical Morphology in Image Processing*, E. R. Dougherty, Ed. New York: Marcel Dekker, 1992, pp. 171–203.

[24] R. C. Gonzalez and R. E. Woods, *Digital Image Processing*. New York: Addison-Wesley, 1993.

[25] D. A. Lauffenburger and A. F. Horwitz, "Cell migration: A physically integrated molecular process," *Cell*, vol. 84, pp. 359–369, 1996.

[26] J. A. Cooper, "Effects of cytochalasin and phalloidin on actin," *J. Cell Biol.*, vol. 105, pp. 1473–1478, 1987.